electronics

MDPI

Communication

A 237 GHz Traveling Wave Tube for Cloud Radar

Ying Li, Pan Pan, Bowen Song, Lin Zhang and Jinjun Feng *

National Key Laboratory of Science and Technology on Vacuum Electronics, Beijing Vacuum Electronics Research Institute, Beijing 100015, China; ly-buct@hotmail.cn (Y.L.)
* Correspondence: fengjinjun@tsinghua.org.cn; Tel.: +86-18046510463

Abstract: In this article, the first 237 GHz traveling wave tube (TWT) is presented as a high-power amplifier for the terahertz (THz) cloud radar. As is common with previous G-band traveling wave tubes developed at Beijing Vacuum Electronics Research Institute, the 237 GHz traveling wave tube employs a 20 kV, 50 mA pencil electron beam focused using periodic permanent magnets (PPMs) to achieve compactness. A folded waveguide (FWG) slow-wave structure (SWS) with modified circular bends is optimized to provide high impedance and eliminate sideband oscillations. Limited by insufficient drive power, this device is not saturated. The measured maximum output power and gain are 8.9 W and 35.7 dB, and the 3 dB gain bandwidth achieves 4 GHz.

Keywords: vacuum electronic amplifier; traveling wave tube; folded waveguide

1. Introduction

Cloud radar systems play a significant role in the study of clouds and precipitation [1]. The W-band space-borne CloudSat Cloud Profiling Radar has had great success in sampling clouds worldwide since it was launched in 2006 by the National Aeronautics and Space Administration (NASA) [2]. Higher radar frequencies have not been used yet, but with the continuous development of THz source technology, THz imaging technology exhibits important potential in cloud monitoring applications, since it has the advantage of high gain from small apertures, as well as higher sensitivity and accuracy, by offering an attractive solution for dual-wavelength measurements at small particle sizes and for water vapor profiling [3]. Considering maturity and rain attenuation, G-band is the most promising frequency for the next generation of cloud radar systems. Robert and James developed a 215 GHz radar system and successfully obtained the cloud and vertical profile up to several km with ground experiment [4]. CPI has developed a 263 GHz high-power pulsed amplifier also intended for advanced weather radar [5]. A G-band space-borne cloud radar project is supported by the National Natural Science Foundation of China. To avoid other application frequencies such as 220 GHz for communications, 237 GHz was chosen as the center frequency of this radar, which drives the need for a compact 237 GHz power amplifier with a 2 GHz bandwidth of output power over 5 W.

Vacuum electronic devices (VEDs) exhibit the highest average power in the THz frequency range [6]. TWTs, especially equipped with PPMs [7], have the advantage of moderate power, wide instantaneous bandwidth, portability, and compact size [8,9]. G-band TWTs with over 50 W output power have been developed, but these devices require high input power and employ bulky, uniform, permanent magnets [10,11]. Compared with those devices, PPM-focused G-band TWTs provide lower power but have advantages regarding volume and weight [12–14].

As the crucial part of a TWT, the SWS largely determines the amplifier's performance. The FWG SWS has been widely used in THz TWTs, and it is capable of high-power wideband performance and proves less sensitive to fabrication uncertainties [12–16]. As an improvement of the FWG SWS, the FWG SWS with modified circular bends has the advantages of higher coupling impedance and sideband stability [17]. The design and

check for updates

Citation: Li, Y.; Pan, P.; Song, B.; Zhang, L.; Feng, J. A 237 GHz Traveling Wave Tube for Cloud Radar. *Electronics* **2023**, *12*, 2153. https://doi.org/10.3390/electronics12102153

Received: 24 March 2023
Revised: 4 May 2023
Accepted: 5 May 2023
Published: 9 May 2023

Copyright: © 2023 by the authors. Licensee MDPI, Basel, Switzerland. This article is an open access article distributed under the terms and conditions of the Creative Commons Attribution (CC BY) license (https://creativecommons.org/licenses/by/4.0/).

demonstration of a 237 GHz TWT utilizing the FWG SWS with circular bends and PPMs are described in this paper, which is organized as follows. In Section 2, systems designs including SWS, Electron Optical, and energy transmission systems are presented. In Section 3, the performance of the 237 GHz TWT is illustrated. Finally, Section 4 offers conclusions.

2. Systems Design

The building blocks of the 237 GHz TWT are shown in Figure 1. A FWG SWS with circular bends is specifically optimized to not only achieve the target power and bandwidth but also maintain operational stability. A 20 kV, 50 mA Pierce electron gun, a PPM focusing system, and a single-stage depressed collector compose the electron optical system in order to emit, concentrate, and collect electrons. In addition, RF windows are employed to achieve energy coupling and transmission of the TWT. The three components are described below separately.

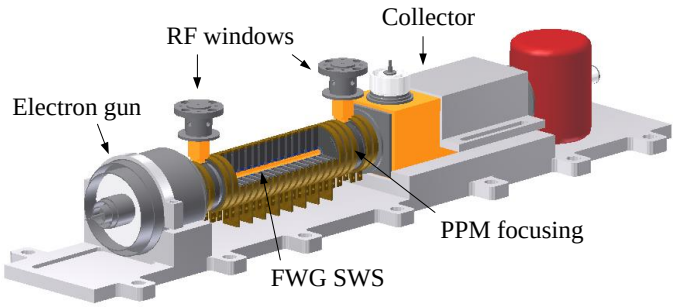

Figure 1. Building blocks of the 237 GHz TWT.

a. SWS Design

Figure 2 shows the schematic of the normal FWG SWS and the FWG SWS with modified circular bends, where r is the radius of the electron beam channel; P is the period length of the SWS; a, b, and h are the width, height, and length of the waveguide separately; and R_{in}, R_{out} is the radius of the inner arc and outer separately. In a normal FWG SWS, the inner and outer arcs are concentric. The FWG SWS with modified circular bends is different from the norm in that the center of the outer arc (O_{out}) is shifted outward. The geometrical dimensions of the two 237 GHz circuits are listed in Table 1.

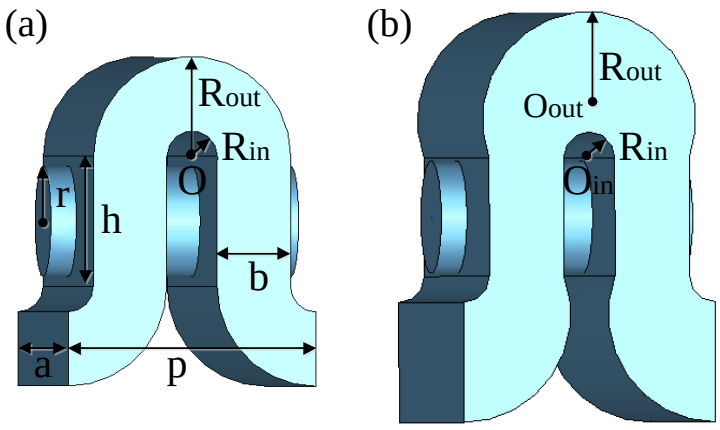

Figure 2. Structure models of (**a**) normal FWG SWS and (**b**) FWG SWS with modified circular bends.

Table 1. Geometrical Parameters.

Symbol	Geometric Parameters	Normal FWG SWS	FWG SWS with Modified Circular Bends
p (μm)	Period Length	532	540
b (μm)	Height of Waveguide	160	160
a (μm)	Width of Waveguide	760	760
h (μm)	Length of Waveguide	240	240
r (μm)	Beam Channel Radius	120	120
R_{out} (μm)	Outer Radius	213	300
R_{in} (μm)	Inner Radius	55	55
$O_{out} - O_{in}$ (μm)	Distance of the Arc Center	0	30

The cold characteristics of the SWS were simulated by using the CST Microwave Studio Eigenmode Solver [18]. Figure 3 shows the dispersion curve of the normal FWG SWS and the FWG SWS with modified circular bends. The two modes represent two propagation modes of the electromagnetic waves in the SWSs, respectively. In both SWS circuits, the 20 kV beam line intersects with the fundamental mode near 237 GHz, and $f_{center}/f_{cut-off} \approx 1.16$ allows for excellent beam–wave synchronization near the f_{center}. However, since the period of the SWS is limited by the processing capacity of CNC machining, the SWS tends to operate at a higher voltage. In the normal FWG SWS, the beam line will intersect with the second order mode near the 4π point (720°) where it has a strong electric field in the beam channel (axis Z) as shown in Figure 3a, causing a potential backward-wave oscillation. The modified circular bends eliminate the oscillation by reducing the 4π frequency and making the electric field near zero in the beam channel of the second order mode as shown in Figure 3b.

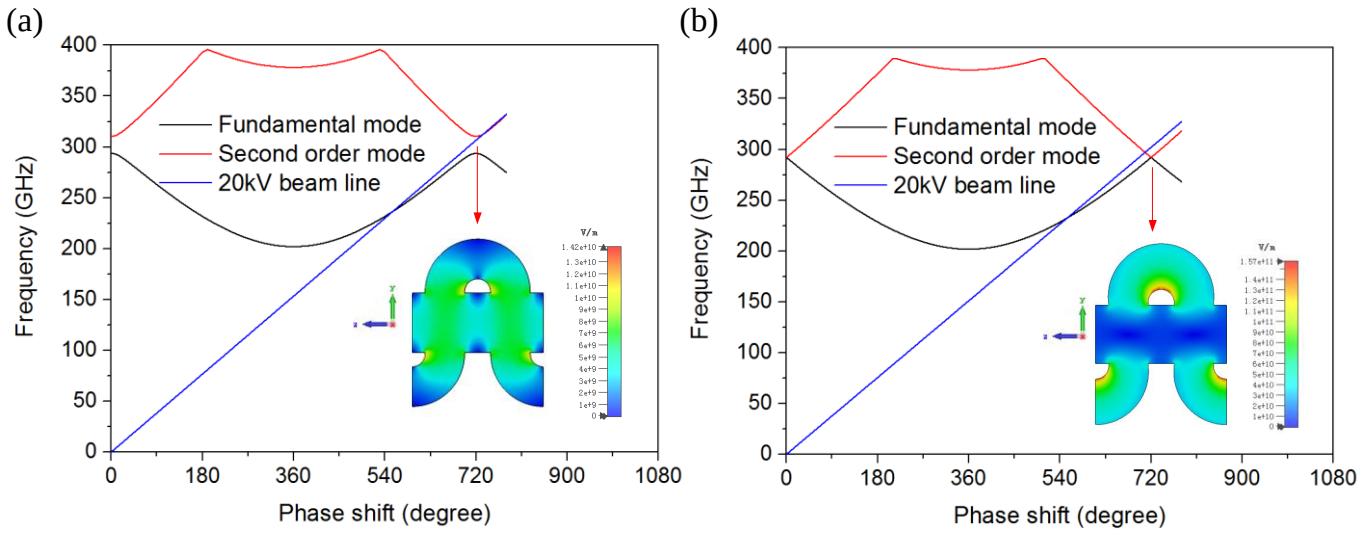

Figure 3. Dispersion curves of (**a**) FWG SWS and (**b**) FWG SWS with modified circular bends of the 237 GHz TWT.

Figure 4 shows the normalized phase velocity and coupling impedance of these two SWSs. It can be seen that the FWG SWS with modified circular bends increased the coupling impedance by more than 12% compared to the normal FWG SWS while maintaining approximately the same phase velocity. In the optimized SWS, the difference in phase velocity was less than 0.55% of Vp/c (center), and the coupling impedance was over 0.92 Ω in 235–239 GHz. The effective conductivity of the SWS was empirically set as 2.1×10^7 S/m considering the surface roughness of about 0.2 μm [19], and the corresponding loss was about 220 dB/m.

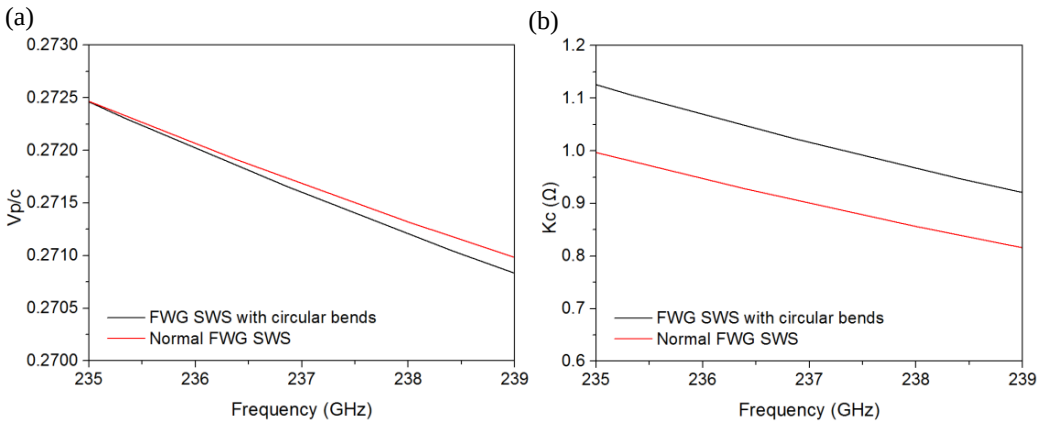

Figure 4. The (**a**) normalized phase velocity and (**b**) coupling impedance of the FWG SWS and FWG SWS with modified circular bends.

The beam–wave interaction performance of the SWS circuit was simulated by using the 3D fully electromagnetic particle-in-cell code CST Particle Studio. A 65-period input section and a 75-period output section were separated by a lossy sever, maintaining stable operation while providing over 33 dB gain with low ripples. The simulation model is shown in Figure 5. The electron beam of 20 kV and 50 mA was emitted from a PEC circular plane with a 0.06 mm radius and was focused using a PPM field with a 0.6 T peak value. Figure 6 shows the saturation output power and saturation gain from 235 GHz to 239 GHz. The maximum saturation power in the band was 13.5 W, the minimum saturation power was 10.9 W, and the saturation power fluctuation was 0.9 dB. The maximum saturation gain was 35.3 dB, the minimum saturation gain was 34.3 dB, and the fluctuation of saturation gain was 1 dB. The in-band power and gain consistency are quite good.

The FWG SWS with modified circular bends was precisely fabricated using CNC machining in oxygen-free copper, and the dimensional process accuracy reached 3 μm.

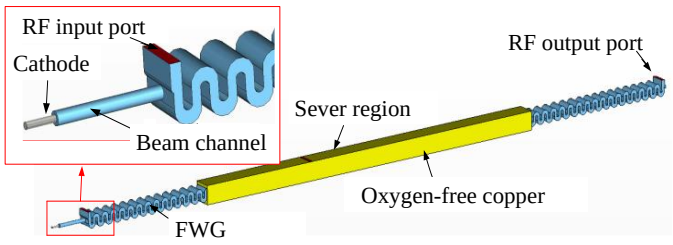

Figure 5. Simulation model of SWS circuit.

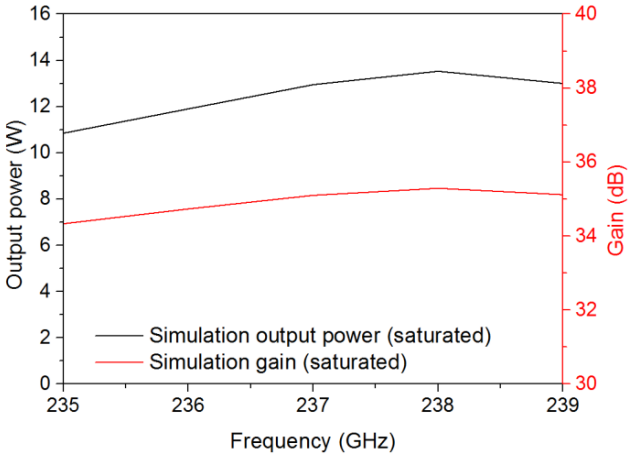

Figure 6. Simulation results of SWS circuit.

b. Electron Optical System

The Pierce electron gun adopts an M-type cathode with a 5 A/cm^2 load. A focus electrode and an anode were used to form the pencil beam and compress the current density to more than 200 A/cm^2. The focus electrode modulated the beam allowing a duty cycle from 0.1% to continuous wave, while the anode could be used to adjust the beam current and transmission ratio.

To focus the electron beam, the peak value of the PPM field should be over two times that of the Brillouin magnetic field (B_b), which is used to quantify the required magnetic field strength under the Brillouin condition [20]:

$$B_b \approx \frac{0.833\sqrt{I_{beam}}}{r_{beam}U_{beam}^{0.25}} \quad (1)$$

The PPM focusing system in this TWT used samarium cobalt magnets and iron pole pieces to produce an on-axis Bz of 0.6 T peak value as shown in Figure 7 calculated using a CST 3D particle magnetic field solver. According to (Equation (1)), the cathode should be magnetic-shielded to minimize the Brillouin magnetic field. The shell of the electron gun is made of Fe-cobalt-nickel alloy material with high magnetic permeability to realize magnetic shielding in the cathode area, and the simulation results show the magnetic field strength on the cathode surface was only 1.15 Gs. The CST 3D particle tracking code demonstrates that this electron optical system can produce and transmit a 20 kV, 50 mA pencil beam with a 0.06 mm average radius through a beam tunnel with a 0.12 mm radius and 100 mm length. The simulated beam transmission ratio reached 99%.

A single-stage depressed collector with an efficiency of 75% was used in the TWT. The distribution of electron trajectories inside the collector is shown in Figure 8. The reflux current was 0 under the design voltage of 17 kV. The temperature distribution of the collector under a 10% duty cycle was simulated using the ANSYS Thermal analysis module [21] as shown in Figure 9. The results show that the maximum temperature of the outer surface was about 56.6 °C, and the maximum temperature of the inner surface was about 93.9 °C. The maximum heat flux was 85 W/cm^2 under conduction cooling conditions, illustrating that the collector can operate stably.

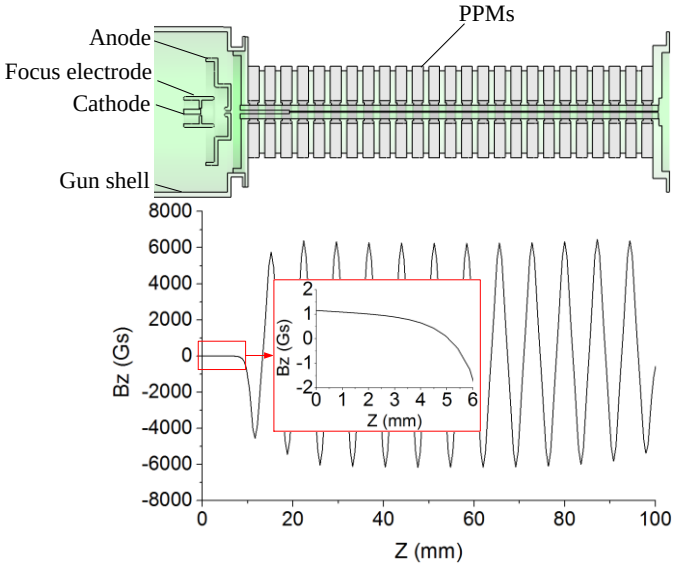

Figure 7. Model and magnetic field distribution of electron optical system.

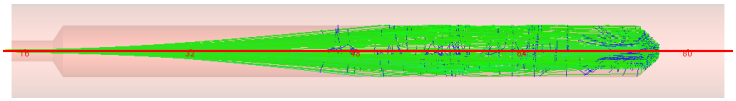

Figure 8. Electron trajectories of single-stage depressed collector.

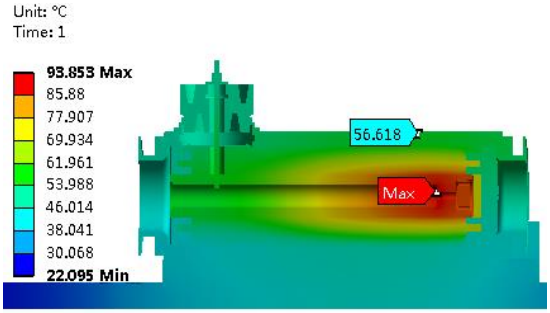

Figure 9. Temperature distribution of single-stage depressed collector.

c. Energy Transmission System

Both the input and output RF windows use the WR4.3 standard waveguide pillbox structure with a chemical vapor deposition (CVD) diamond disc as the dielectric [22]. The diamond disc was metalized using a composite coating process and sealed with a Fe-cobalt-nickel alloy window frame to form the RF window, thus maintaining the vacuum atmosphere of the tube while achieving low reflection over a broad bandwidth. Figure 10 shows the comparison between the measured and simulated S-parameters of an RF window. Considering errors of processing and assembly, the measured results are in good agreement with the simulated results. The measured insertion loss of a typical RF window was about −1 dB, and the reflection (S11) was lower than −15 dB from 200 GHz to 240 GHz, covering the 235–239 GHz frequency band.

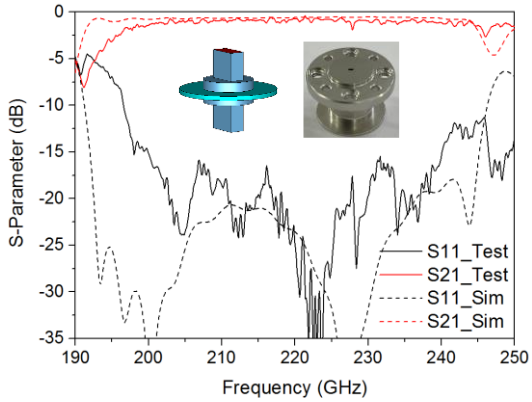

Figure 10. CVD pill-box window and its S-parameters.

3. TWT Performance

Figure 11 is the prototype of the 237 GHz TWT. The weight and the size of the TWT are 2 kg and 300 mm × 70 mm × 70 mm, respectively. The TWT operating voltage was 20.5 kV, and the emission current was 50 mA. After debugging, the collector current was 46.7 mA, and the corresponding electron beam transmission ratio is 93%. No oscillation was observed during the test at 10% duty cycle.

The block diagram and the hot test platform of the experimental setup are shown in Figure 12. A solid-state amplifier multiplier chain (AMC) was used as the driven source of the TWT. The TWT output power was measured with a directional coupler and a THz power meter.

The measured results are shown in Figure 13. Compared with the required drive power 7 dBm, the power of the available solid-state AMC was too low to drive the TWT saturation as shown in Figure 13a. The measured output power and gain of the TWT are shown in Figure 13b. The maximum output power was 8.9 W at 236 GHz, and the maximum gain was 35.7 dB at 236.8 GHz, respectively. Though the drive power was insufficient to saturate the TWT, especially in 237–238 GHz, the output power exceeded 8 W over 2.7 GHz bandwidth. The widest measured 3 dB bandwidth of the TWT achieved 4 GHz, and the bandwidth of gain over 30 dB was more than 6.6 GHz covering 233.6–239.2 GHz.

The measured gain of the TWT was compared with the simulation results, as shown in Figure 14. The insertion losses of the input window and the output window were both estimated as −1 dB in the simulation, which had been verified by the cold test as shown in Figure 11. The measured unsaturated gain was about 2–3 dB higher than the simulated saturation gain. Considering that the saturation gain was slightly lower than the small-signal gain, the measured results and the simulation results are in good agreement, which demonstrates that the output power of the TWT will achieve the design target under sufficient input power. During the experiment, the highest temperature of the outer surface of the collector was 58.5 °C as shown in Figure 15, which was consistent with the simulation result.

The performance parameters of this tube and other G-band TWTs are summarized in Table 2. This device takes advantage of the PPM focusing scheme to achieve compactness and light weight. To maintain a high electron beam transmission level, the same beam channel size and total current as in reference [14] were used. Experimental results show that with the SWS carefully designed in this tube, the circuit can achieve a higher gain at a higher frequency band while adopting the same beam channel size. It is worth noting that the SWS in this tube is a homogeneous circuit, and the phase velocity tapering technique in reference [13] can be used to further improve the power and gain.

This tube will be followed by cloud radar experiments with a sufficient power source.

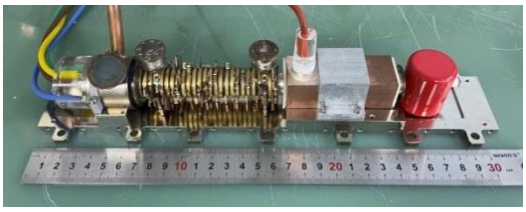

Figure 11. Prototype of the 237 GHz TWT.

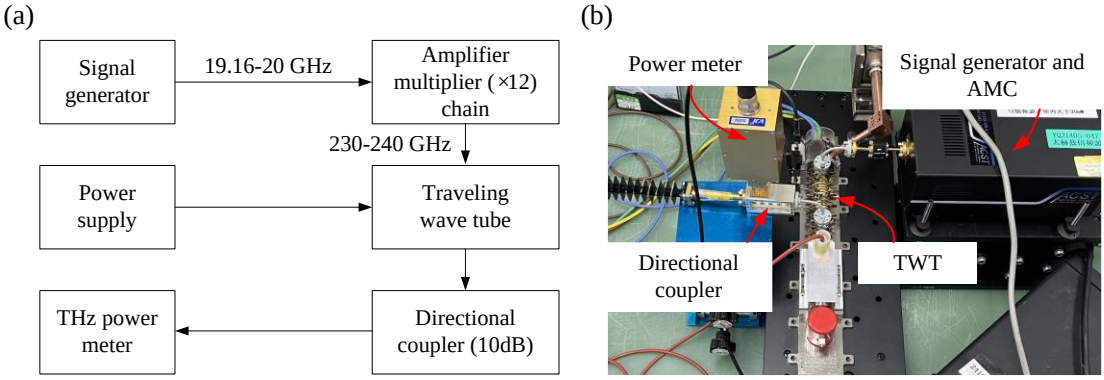

Figure 12. The (**a**) block diagram and (**b**) hot test platform of the experimental setup.

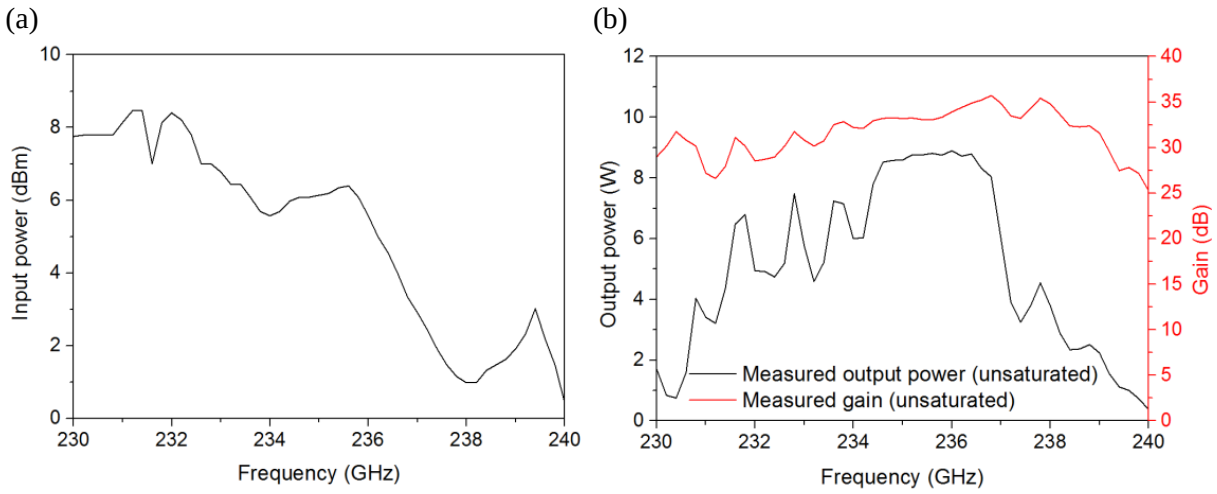

Figure 13. Measured results of (**a**) solid-state AMC's power and (**b**) TWT's output power and gain.

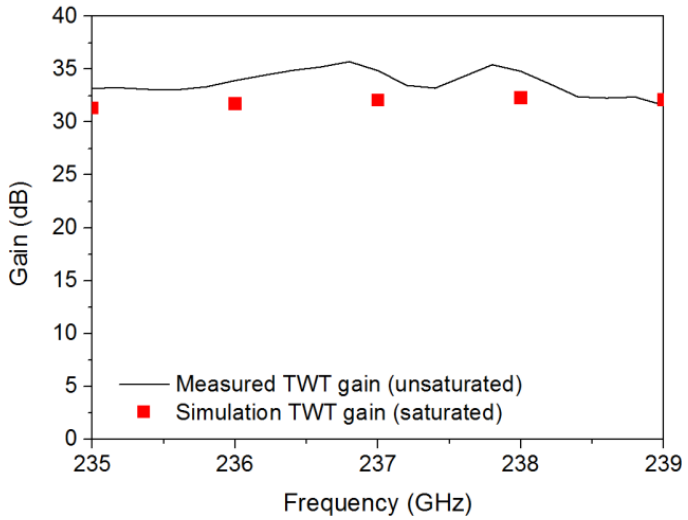

Figure 14. Comparison of the measured gain and the simulation results of the TWT.

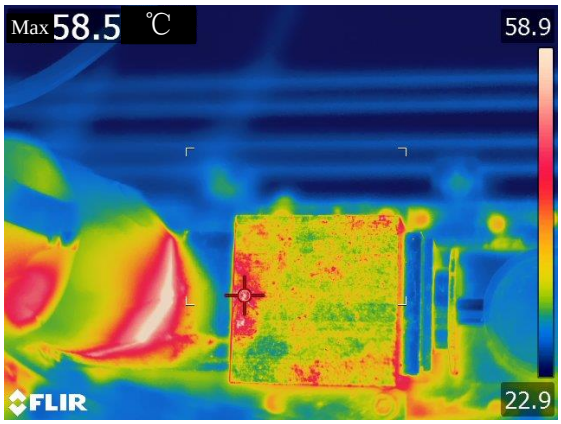

Figure 15. Temperature of the collector outer surface.

Table 2. Performance of G-band TWTs.

Frequency (GHz)	Power (W)	Gain (dB)	Focusing
232.4–234.8 [10]	50	23	Uniform Permanent Magnets
214.5 [11]	63	8	Uuniform Permanent Magnets
232–234.5 [12]	16	30	PPMs
215.4–219 [13]	50	35	PPMs
214–221.6 [14]	15	32	PPMs
236 (This Device)	8.9 (Unsaturated)	34	PPMs

4. Conclusions

The first compact 237 GHz TWT with a pencil beam focused using PPMs has been designed and developed aimed at a G-band cloud radar. To ensure the amplifier's practical performance, the geometric parameters of its high-frequency structure have been carefully tuned to balance gain and bandwidth while avoiding sideband oscillation. Limited by insufficient power from the available solid-state driver, the measured maximum out-of-window power and gain of this tube are 8.9 W and 35.7 dB separately. The output power exceeds 8 W over 2.7 GHz bandwidth, and the 3 dB gain bandwidth achieves 4 GHz. Further experiments will be carried out with the tube.

Author Contributions: Conceptualization, P.P. and J.F.; methodology, P.P.; software, Y.L.; validation, Y.L., B.S. and L.Z.; formal analysis, P.P.; investigation, Y.L.; resources, J.F.; data curation, Y.L.; writing—original draft preparation, Y.L.; writing—review and editing, Y.L.; visualization, P.P.; supervision, J.F.; project administration, J.F.; funding acquisition, J.F. All authors have read and agreed to the published version of the manuscript.

Funding: This research was funded by National Natural Science Foundation of China under Grant 61527805.

Data Availability Statement: No new data were created or analyzed in this study. Data sharing is not applicable to this article.

Conflicts of Interest: The authors declare no conflict of interest.

References

1. Sassen, K.; Wang, Z. Classifying clouds around the globe with the CloudSat. *Geophys. Res. Lett.* **2008**, *35*, L04805. [CrossRef]
2. Walker McLinden, M.L.; Li, L.; Heymsfield, G.M.; Coon, M.; Emory, A. The NASA GSFC 94-GHz Airborne Solid-State Cloud Radar System (CRS). *J. Atmos. Ocean. Technol.* **2021**, *38*, 1001–1017. [CrossRef]
3. Battaglia, A.; Kollias, P.; Dhillon, R.; Roy, R.; Tanelli, S.; Lamer, K.; Grecu, M.; Lebsock, M.; Watters, D.; Mroz, K.; et al. Spaceborne Cloud and Precipitation Radars: Status, Challenges, and Ways Forward. *Rev. Geophys. Adv. Earth Space Sci.* **2020**, *58*, e2019RG000686. [CrossRef] [PubMed]
4. McIntosh, R.; Narayanan, R.; Mead, J.; Schaubert, D. Design and performance of a 215 GHz pulsed radar system. *IEEE Trans. Microw. Theory Tech.* **1988**, *36*, 994–1001. [CrossRef]
5. Hyttinen, M.; Roitman, A.; Horoyski, P.; Deng, H. High Power Pulsed 263 GHz Extended Interaction Amplifier. In Proceedings of the 2020 IEEE 21st International Conference on Vacuum Electronics (IVEC), Monterey, CA, USA, 19–22 October 2020; pp. 1–2. [CrossRef]
6. Armstrong, C.M. The truth about terahertz. *IEEE Spectr.* **2012**, *49*, 36–41. [CrossRef]
7. Mendel, J.T.; Quate, C.F.; Yocom, W.H. Electron beam focusing with periodic permanent magnet fields. *Proc. IRE* **1954**, *42*, 800–810. [CrossRef]
8. Sherwin, M. Terahertz power. *Nature* **2002**, *420*, 131–133. [CrossRef] [PubMed]
9. Booske, J.H.; Dobbs, R.J.; Joye, C.D.; Kory, C.L.; Neil, G.R.; Park, G.-S.; Park, J.; Temkin, R.J. Vacuum Electronic High Power Terahertz Sources. *IEEE Trans. Terahertz Sci. Technol.* **2011**, *1*, 54–75. [CrossRef]
10. Basten, M.; Tucek, J.; Gallagher, D.; Kreischer, K. 233 GHz high power amplifier development at Northrop Grumman. In Proceedings of the 2016 IEEE International Vacuum Electronics Conference (IVEC), Monterey, CA, USA, 19–21 April 2016; pp. 1–2. [CrossRef]
11. Joye, C.D.; Kimura, T.; Hyttinen, M.; Levush, B.; Cook, A.M.; Calame, J.P.; Abe, D.K.; Vlasov, A.N.; Chernyavskiy, I.A.; Nguyen, K.T.; et al. Demonstration of a high power, wideband 220-GHz traveling wave amplifier fabricated by UV-LIGA. *IEEE Trans. Electron Devices* **2014**, *61*, 1672–1678. [CrossRef]

12. Armstrong, C.M.; Kowalczyk, R.; Zubyk, A.; Berg, K.; Meadows, C.; Chan, D.; Schoemehl, T.; Duggal, R.; Hinch, N.; True, R.B.; et al. A Compact Extremely High Frequency MPM Power Amplifier. *IEEE Trans. Electron Devices* **2018**, *65*, 2183–2188. [CrossRef]
13. Bian, X.; Pan, P.; Tang, Y.; Lu, Q.; Li, Y.; Zhang, L.; Wu, X.; Cai, J.; Feng, J. Demonstration of a Pulsed G-Band 50-W Traveling Wave Tube. *IEEE Electron Device Lett.* **2020**, *42*, 248–251. [CrossRef]
14. Pan, P.; Tang, Y.; Bian, X.; Zhang, L.; Lu, Q.; Li, Y.; Feng, Y.; Feng, J. A G-Band Traveling Wave Tube with 20 W Continuous Wave Output Power. *IEEE Electron Device Lett.* **2020**, *41*, 1833–1836. [CrossRef]
15. YFeng, Y.; Bian, X.; Song, B.; Li, Y.; Pan, P.; Feng, J. A G-Band Broadband Continuous Wave Traveling Wave Tube for Wireless Communications. *Micromachines* **2022**, *13*, 1635. [CrossRef]
16. Hu, P.; Lei, W.; Jiang, Y.; Huang, Y.; Song, R.; Chen, H.; Dong, Y. Demonstration of a Watt-Level Traveling Wave Tube Amplifier Operating Above 0.3 THz. *IEEE Electron Device Lett.* **2019**, *40*, 973–976. [CrossRef]
17. Cai, J.; Feng, J.; Wu, X. Folded Waveguide Slow Wave Structure with Modified Circular Bends. *IEEE Trans. Electron Devices* **2014**, *61*, 3534–3538. [CrossRef]
18. CST Particle Studio. CST Computer Simulation Technology GmBH. [Online]. Available online: http://www.cst.com (accessed on 10 March 2020).
19. Pan, P.; Li, H.; Feng, J. Study on loss of folded waveguide structures of 220 GHz and 340 GHz. In Proceedings of the 2016 IEEE International Vacuum Electronics Conference (IVEC), Monterey, CA, USA, 19–21 April 2016; pp. 1–2. [CrossRef]
20. Gilmour, J.A.S. *Klystrons, Traveling Wave Tubes, Magnetrons, Crossed-Filed Ampliers, and Gyrotrons*; Artech House: Norfolk County, MA, USA, 2011.
21. Zienkiewicz, O.C.; Taylor, R.L.; Zhu, J.Z. *The Finite Element Method: Its Basis and Fundamentals*; Elsevier: Amsterdam, The Netherlands, 2005.
22. Ding, M.Q.; Li, L.; Feng, J. A study of high-quality freestanding diamond films grown by MPCVD. *Appl. Surf. Sci.* **2012**, *258*, 5987–5991. [CrossRef]

Disclaimer/Publisher's Note: The statements, opinions and data contained in all publications are solely those of the individual author(s) and contributor(s) and not of MDPI and/or the editor(s). MDPI and/or the editor(s) disclaim responsibility for any injury to people or property resulting from any ideas, methods, instructions or products referred to in the content.